CHINESE OPTICS LETTERS

Vol. 22, No. 12 | December 2024

Electrically controlled light focusing by a tunable metasurface using thin film lithium niobate

Haoyu Wang (王昊昱)[1], Zhancheng Li (李占成)[1*], Wenwei Liu (刘文玮)[1], Yuebian Zhang (张跃变)[1], Hua Cheng (程 化)[1**], and Shuqi Chen (陈树琪)[1,2,3***]

[1] Key Laboratory of Weak Light Nonlinear Photonics, Ministry of Education, School of Physics and TEDA Institute of Applied Physics, Nankai University, Tianjin 300071, China

[2] School of Materials Science and Engineering, Smart Sensing Interdisciplinary Science Center, Nankai University, Tianjin 300350, China

[3] Collaborative Innovation Center of Extreme Optics, Shanxi University, Taiyuan 030006, China

*Corresponding author: zcli@nankai.edu.cn

**Corresponding author: hcheng@nankai.edu.cn

***Corresponding author: schen@nankai.edu.cn

Received January 24, 2024 | Accepted June 13, 2024 | Posted Online December 24, 2024

We theoretically demonstrate electrically controlled light focusing using a tunable metasurface employing thin film lithium niobate (TFLN). The designed metasurface features a high-quality factor guided-mode resonance with an electrically controllable resonant wavelength, resulting in a high extinction ratio of transmittance at the operational wavelength by changing the applied voltage. A reconfigurable one-dimensional Fresnel zone plate with a focusing efficiency of around 15% has been realized through spatial modulation of transmitted light intensity, whose focal position can be electrically tunable in both longitudinal and lateral directions. Our approach reveals the great potential of metasurfaces using TFLN for electrically controlled light focusing.

Keywords: metasurface; thin film lithium niobate; electrically controlled light focusing; electro-optical Pockels effect.
DOI: 10.3788/COL202422.123601

1. Introduction

The optical lens has found extensive application in a wide range of optical systems and serves as a fundamental component for numerous cutting-edge technologies. The traditional optical lens, which is designed by utilizing various materials to engineer the spatial distribution of the refractive index, is inevitably bulky. This inherent limitation poses challenges for integrating such lenses into compact devices or systems. Metasurface lenses, known as metalenses, exhibit compactness and offer versatile functionalities in comparison with conventional lenses[1]. They have demonstrated significant applications in subwavelength resolution imaging, polarimetric beam profiling, and other related fields[2–4]. A current research focus in the field of metalenses is the realization of dynamic manipulation of light focusing, which plays a critical role in augmented and virtual reality, microscopy, and optical communication. Dynamically tunable or reconfigurable metalenses have been effectively demonstrated utilizing stretchable substrates[5], actuated lens doublets[6], mechanical systems[7,8], and the employment of active materials[9–11]. Despite these remarkable approaches, the modulation depth and speed of reconfigurable metalenses still require further improvement.

Lithium niobate (LN) has emerged as an excellent alternative for the implementation of integrated photonic devices due to its wide transparency, high refractive index, significant electro-optic coefficient, and remarkable chemical and mechanical stability[12,13]. Especially, LN and other ferroelectric materials have been widely used for the implementation of electro-optic modulators at the microscale since the Pockels effect they supported can change the refractive index of LN at an extremely high speed up to ~100 GHz[14–19]. Photonic crystals with a high local field factor were reported to enhance the electro-optic effect with a substantially larger refractive index change (on the order of 10^{-1}) compared to that predicted by the classical Pockels effect in bulk LN material ($\sim 10^{-2}$)[20–24]. On the other hand, reconfigurable metasurfaces have emerged as a powerful platform for dynamic manipulation of optical waves[25,26]. Metasurfaces employing thin film lithium niobate (TFLN) for modulating free-space light utilize high-quality (Q) factor resonance to improve the modulation efficiency[27]. Recent advancements have demonstrated the capability of metasurfaces using TFLN to dynamically manipulate the phase and amplitude of free-space optical fields, thereby offering promising prospects for optical switching and reconfigurable wavefront control[27–34].

Lately, some attempts have been made to electrically control the focusing of light. A metasurface using TFLN has been utilized to realize an active Fresnel zone plate (FZP) with a fixed focal length and electrically controllable focusing efficiency[35]. Further investigation is required to explore the realization of electrically controlled focusing by metasurfaces using TFLN.

Here, we propose a one-dimensional (1D) reconfigurable FZP based on a tunable metasurface using TFLN, whose focal position can be electrically manipulated in both longitudinal and lateral directions. The electrically controlled light focusing is attributed to the 1D spatial manipulation of transmitted light intensity, enabled by the electro-optical Pockels effect of the LN and the high-Q factor of the guided-mode resonance (GMR). By spatially applying different voltages along one direction, the focal position of the FZP with a focusing efficiency of around 15% can be longitudinally tuned in a range of approximately $4800 \times \lambda_0$, accompanied by a tunable lateral displacement equivalent to 50% of the designed metasurface width. Our approach provides a good candidate for the realization of electrically controlled light intensity manipulation and light focusing.

2. Metasurface Design

The designed metasurface is illustrated in Fig. 1(a). The unit cells of the designed metasurface are composed of elliptical cylinders made of titanium dioxide (TiO_2) on a z-cut TFLN, and the elliptical cylinders in different unit cells are interconnected by TiO_2 nanorods along the x-direction. The structural parameters of the TiO_2 nanostructures are $P_x = P_y = 400$ nm, $r_x = 100$ nm, $r_y = 150$ nm, and $w = 50$ nm. The thicknesses of the TiO_2 nanostructure and the TFLN are designed as $t_1 = 80$ nm and $t_2 = 540$ nm, respectively. The indium tin oxide (ITO) layers with a thickness of $t_3 = 17$ nm, which serve as electrostatic contacts, are added onto the top surface of each TiO_2 nanostructure and the bottom surface of the TFLN to enable the application of distinct voltages along the y-axis. This electrode fabrication method has been experimentally and theoretically employed in previous studies[27,36]. The voltages are applied to the ITO layer on the top surface of each column of the TiO_2 nanostructure, while the bottom ITO layer functions as a reference electrode. Consequently, the application of positive voltage induces a decrease in the refractive index of LN. The substrate is made of SiO_2. The unit cells in which TiO_2 elliptical cylinders are connected by TiO_2 nanorods can be applied to the same voltage, while different voltages can be applied to each column of unit cells. The designed metasurface can realize 1D spatial manipulation of transmitted light intensity at the operational wavelength by changing the distribution of applied voltage $V(y)$, resulting in electrically controlled light focusing. In order to achieve electrically controlled 1D spatial manipulation of transmitted light intensity, a high modulation extinction ratio with a small change of the applied voltage is desired. Simultaneously, the inter-electrode distances should be minimized. Therefore, the structural parameters of the designed metasurface are optimized to achieve a high-Q factor GMR with a high extinction ratio within the waveband of 800–900 nm. The operational waveband is selected to align with the latest relevant research[32,34,35]. Given the fixed period of unit cells at 400 nm in both the x- and y-directions, we systematically vary the remaining design parameters individually through iterative sweeps to determine the structural parameters that enable a high modulation extinction ratio for the designed metasurface while minimizing changes in applied voltage. The metasurface acting as a 1D reconfigurable FZP is designed to have 1000 unit cells in the y-direction, serving as an illustrative example that can be realistically chosen alternatively. The commercially available software COMSOL Multiphysics was utilized to simulate the optical responses of the designed metasurface. In the simulation, the SiO_2 is regarded as a lossless material with a refractive index of 1.46. The optical constants of LN, TiO_2, and ITO are taken from experimental data[37–39].

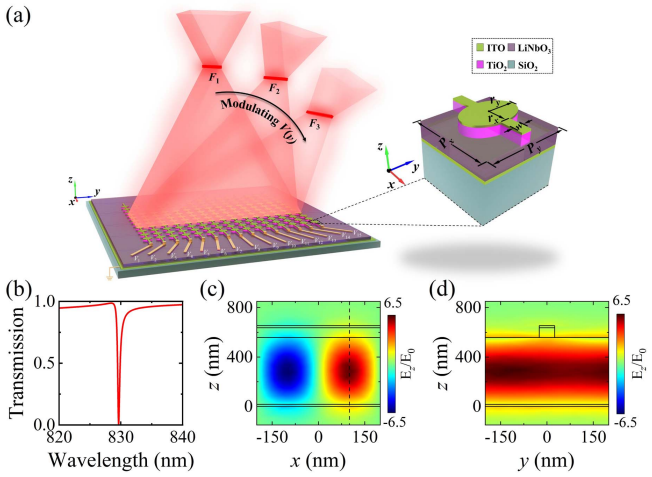

Fig. 1. (a) Schematic of the designed metasurface acting as a reconfigurable 1D FZP with varying focal positions in both longitudinal and lateral dimensions and its unit cell. Characterization of the GMR in the designed metasurface. (b) Transmission spectrum under x-polarized normal incidence. Distribution of the real part of electric field E_z in the (c) x–z plane ($y = 0$ nm) and (d) y–z plane [$x = 100$ nm, marked by the black dashed line in (c)] at the resonant wavelength λ_0.

3. Results and Discussion

For simplicity, we employed simulated results from a single unit cell with periodic boundary conditions to characterize the resonance in the designed metasurface. The transmission spectrum of the designed metasurface under x-polarized normal incidence is illustrated in Fig. 1(b). A sharp transmission dip with a Q factor equal to 1929.4 can be observed at $\lambda_0 = 829.65$ nm, indicating a strong coupling between the incident light and the designed metasurface. This sharp dip is caused by a TM mode GMR, which is a stationary mode resulting from the interference between two counter-propagating waves along the x-direction, as validated by the simulated electric field distributions in

Figs. 1(c) and 1(d). The GMR remains robust even when the structural parameters deviate from their optimized values. For example, the Q factor is primarily influenced by the r_x, whereby a 10 nm increase in r_x results in a reduction of the Q factor to 1633.6. On the other hand, the resonance wavelength is predominantly affected by t_2, with a 10 nm increment leading to a shift of resonant wavelength to 830.8 nm. The variation of the refractive index of the LN also influences the GMR since E_z is enhanced and localized within the TFLN. In order to discuss the influence of the electro-optical Pockels effect on the GMR, we initially simulated the distribution of the electrostatic field when +1 V external voltage is applied to the designed metasurface. The static dielectric constants considered in the electrostatic calculation are taken from Refs. [40,41]. The z component of the electrostatic field E_z^{app} within the TFLN is significantly larger than its x and y components, making it the primary driver of the electro-optical Pockels effect. The simulation results presented in Fig. 2(a) demonstrate a uniform distribution of E_z^{app} throughout the TFLN. Due to the dielectric constant of TiO_2 being larger than that of LN, the electrostatic field is mainly in the LN layer, which overlapps with the optical electrical field and benefits electro-optical modulation. Then, the shifts of the refractive index of the TFLN can be derived by the Pockels first-order derivation:

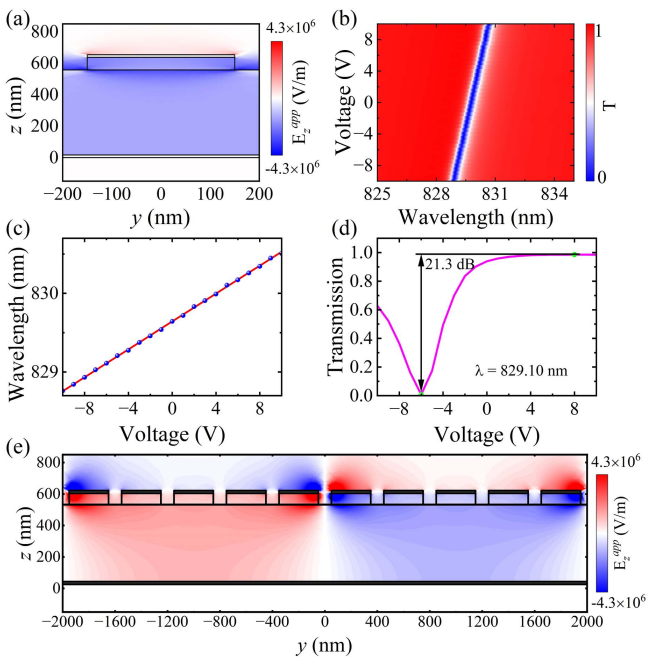

Fig. 2. Electro-optical modulation of the resonance of the designed metasurface. (a) Simulated distribution of the normalized electrostatic field induced by applying a DC voltage of 1 V. (b) The variation of the transmission spectrum as the applied DC voltage changes. The variation of (c) the resonant wavelength and (d) the transmittance at 829.10 nm (resonant wavelength under an external voltage of −6 V) as a function of the applied voltage. The red line in (c) is a linear fit to the simulated data (blue dots). (e) Simulated distribution of the electrostatic field under periodically applied voltage.

$$\Delta n_x = \Delta n_y = -\frac{1}{2} n_o^3 r_{13} E_z^{\mathrm{app}}, \tag{1a}$$

$$\Delta n_z = -\frac{1}{2} n_e^3 r_{33} E_z^{\mathrm{app}}, \tag{1b}$$

where $n_o = 2.2517$ and $n_e = 2.1724$ are the ordinary and extraordinary refractive indices of LN, respectively, and $r_{13} = 10.9$ pm/V and $r_{33} = 34$ pm/V are the electro-optic coefficients of LN[37,40].

Due to the uniform distribution of E_z^{app} throughout the TFLN, we use the average value of E_z^{app} within the TFLN to calculate the shifts of its refractive index[29,31–33]. To investigate the impact of electro-optical Pockels effect-induced shifts in the refractive index of LN on the GMR, we simulated the variation of the transmission spectrum of the designed metasurface as the applied DC voltage changed. As shown in Fig. 2(b), the resonant wavelength redshifts with positive external applied voltage and blue shifts with negative external applied voltage, while the Q factor of the resonance remains unchanged. The relationship between the shifts of the resonant wavelength and the externally applied voltage exhibits a linear correlation, as shown in Fig. 2(c). The linear regression analysis of the data points reveals a tuning sensitivity value of 0.089 nm/V. The obtained modulation efficiency is relatively high, although it does not reach the highest values[27,29,31–33]. The shift follows the relation

$$\frac{\Delta n}{n_0} = \frac{\Delta \lambda}{\lambda_0}, \tag{2}$$

where the resonance wavelength and refractive index, in the absence of applied voltage, are denoted as λ_0 and n_0, respectively. It predicts a tuning sensitivity value of 0.096 nm/V, corresponding to the simulated result. The resonant wavelength can be viewed as a function of multiple variables, determined not only by the refractive index and structural parameters of the TFLN but also by the structural parameters of the TiO_2 nanostructures. Thus, the relationship between the resonance wavelength and refractive index of LN exhibits a deviation from the ideal equation's calculated results. The large sensitivity can be attributed to the high-Q factor resonance and the good overlap of the optical field and electrostatic field. Due to the exceptional tuning sensitivity, a high extinction ratio of transmittance with a value of 21.3 dB [calculated by 10 $\lg(T_{\max}/T_{\min})$] can be achieved, as validated by the results in Fig. 2(d).

The designed metasurface can be used for 1D spatial manipulation of transmitted light intensity by changing the distribution of external applied voltage. The result in Fig. 2(e), illustrating the distribution of the electrostatic field when the specially varied ±1 V voltages are applied to every 5 periods, validates that the external voltage applied to every 5 unit cells along the y-axis can be independently manipulated. To make a proof of the concept, a reconfigurable FZP with a tunable focal position is designed. We choose the center of the designed metasurface as the origin of the coordinate. Then, the distribution of transmission intensity for a designed FZP with a given focal length f can be obtained based on[35]

$$r_i = \sqrt{i\lambda_0 f + \frac{1}{4} i^2 \lambda_0^2}, \tag{3}$$

where r_i represents the radius of the ith zone in the FZP. The o-zones, where i is an odd number, represent regions with high transmittance, while the e-zones, where i is an even number, represent regions with zero transmittance. By varying the externally applied voltage within the range of −6 to 8 V, the transmission intensity of the unit cell at $\lambda = 829.10$ nm can be modulated from 0.0073 to 0.9860, as shown in Fig. 2(d). Therefore, for the unit cells located in o-zones and e-zones, the external applied voltage should be −6 and +8 V, respectively, to obtain the required distribution of transmitted light intensity for light focusing. Moreover, the GMR can be affected by aperiodic boundary conditions. Specifically, Figs. 1(c) and 1(d) validate that the GMR is a stationary mode resulting from the interference between two counter-propagating waves along the x-direction. Thus, the influence of aperiodic boundaries along the y-direction is smaller than that along the x-direction, and this influence can be effectively suppressed by including at least five columns of unit cells in each zone of the designed FZP. For the simulation of light focusing with the designed metasurface, we simulated 1000 unit cells along the y-direction with periodic boundary conditions in the x-direction. Then, we obtained the electric field distribution by sampling at intervals of 400 nm in both x- and y-directions, at a distance of 500 nm above the TFLN. This location is approximately half a wavelength above the metasurfaces, ensuring a uniform electric field distribution. Finally, far-field electric field distributions were calculated using 1D angular spectrum theory. We expanded the array to 1.5 times its original length by filling additional blank areas surrounding it to avoid any influence from boundary effects on the calculated results[42–45].

The longitudinal focal position of the designed FZP can be easily modulated by adjusting the spatial distributions of applied voltages $V(y)$. The simulated results depicted in Fig. 3(a) demonstrate the capability of the designed 1D FZP to effectively modulate its longitudinal focal position within a range spanning from 1 to 6 mm, thereby indicating an impressive tuning depth exceeding $4800 \times \lambda_0$. In order to better show the performance of light focusing, we plot the intensity distribution for $y \in [-100, 100]$ μm, while the length of the designed FZP in the y-direction is 400 μm. We compare the simulated light focusing with the ideal one, for which the transmission intensities of o-zones and e-zones are set to be 0.9860 and 0.0073, respectively. Subsequently, we employ angular spectrum theory to calculate the far-field electric field distributions. In this situation, the near-field interaction within the boundaries of different zones in the FZP is neglected. The designed focal lengths exhibit excellent agreement with the simulated values, as illustrated in Fig. 3(b). Due to the limited size of the designed metasurface, the focusing efficiency (14.6%–17.3%) and the full width at half-maximum (FWHM) (3.0–10.5 μm) of the focal line are dependent on its longitudinal focal position, as shown by the calculated and simulated results in Figs. 3(c) and 3(d). The focusing efficiency is defined as the ratio of the power gathered in a rectangle area with a width of 3× FWHM and a length equal to that of the simulation region and the total power in a square area confined by edges of the simulation region[10,46]. A larger focal length indicates a reduced number of zones in the designed Fresnel zone plate, leading to an increased FWHM. Meanwhile, the presence of different external applied voltages in adjacent unit cells along the y-direction leads to a reduction in focusing efficiency due to nearest-neighbor interaction.

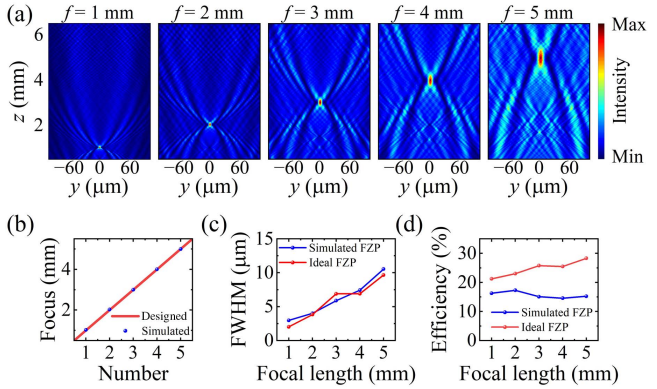

Fig. 3. The implementation of longitudinal reconfigurable light focusing. (a) Simulated intensity distributions of transmitted light in the y–z plane ($x = 0$ nm). (b) The designed and simulated focal lengths for different spatial distributions of applied voltages. The designed and simulated (c) FWHMs and (d) efficiencies of the five focal lines with different focal lengths.

Besides the electrical control of light focusing in the longitudinal direction, the focal position of the designed FZP can also be modulated in the lateral direction by shifting the origin of the coordinate along the y-axis based on Eq. (3). The performance of the designed FZP for electrically controlled light focusing in the lateral direction is also characterized with five different distributions of externally applied voltage $V(y)$, each corresponding to the same longitudinal focal length but with varying lateral shifts.

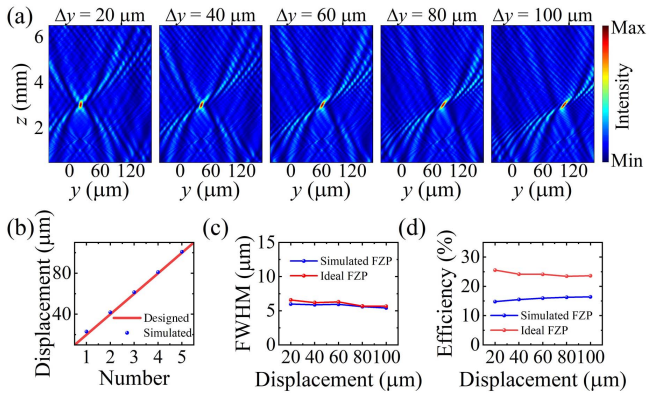

Fig. 4. The implementation of lateral reconfigurable light focusing by adjusting the applied voltages along the y-axis. (a) Simulated intensity distributions of transmitted light in the y–z plane ($x = 0$ nm). (b) The designed and simulated lateral displacements of the focal lines with a longitudinal focal length of 3 mm for different spatial distributions of applied voltages. The designed and simulated (c) FWHMs and (d) efficiencies of the five focal lines with different lateral displacements.

As illustrated in Fig. 4(a), the maximum lateral shift of the focal line is ±100 μm, which is 50% of the designed metasurfaces' width. The designed lateral displacements and the simulated ones are in good agreement, as shown in Fig. 4(b). Different from the results in Figs. 3(c) and 3(d), the FWHM (∼6 μm) of the focal line and the focusing efficiency (∼15%) are almost independent of the lateral displacements, as illustrated in Figs. 4(c) and 4(d). This is reasonable as the number of zones remains constant despite different lateral displacements of the focal line. The simulated focusing efficiency is lower than the designed one due to the neighbor interaction between *o*- and *e*-zones.

4. Conclusion

In conclusion, we proposed a tunable metasurface using TFLN for achieving reconfigurable light focusing by spatially modulating the transmitted light intensity. Taking advantage of the electro-optical Pockels effect of LN and the high-*Q* factor GMR, the resonant wavelength of the GMR can be electrically modulated with a shift rate of 0.089 nm/V. As a result, a high extinction ratio of transmittance can be achieved by changing the applied voltage. Importantly, the applied voltage can be spatially tailored along one direction, enabling spatial manipulation of transmitted light intensity. We have demonstrated that the designed metasurface can function as a 1D reconfigurable FZP, with its focal position being electrically tunable in both longitudinal and lateral directions. Our approach provides an effective alternative for electrical manipulation of light intensity and the realization of reconfigurable light focusing, which can be further applied to optical wavefront manipulation and gray-scale imaging.

Acknowledgements

This work was supported by the National Key Research and Development Program of China (Nos. 2021YFA1400601 and 2022YFA1404501), the National Natural Science Foundation for Distinguished Young Scholars (No. 11925403), the National Natural Science Foundation of China (Nos. 12122406, 12192253, 12274237, 12274239, and U22A20258), and the Natural Science Foundation of Tianjin (Nos. 22JCYBJC01350, 22JCZDJC00400, and 22JCYBJC00800).

References

1. H.-T. Chen, A. J. Taylor, and N. Yu, "A review of metasurfaces: physics and applications," Rep. Prog. Phys. **79**, 076401 (2016).
2. W. T. Chen, A. Y. Zhu, V. Sanjeev, *et al.*, "A broadband achromatic metalens for focusing and imaging in the visible," Nat. Nanotechnol. **13**, 220 (2018).
3. M. Pan, Y. Fu, M. Zheng, *et al.*, "Dielectric metalens for miniaturized imaging systems: progress and challenges," Light Sci. Appl. **11**, 195 (2022).
4. S. Wang, P. C. Wu, V.-C. Su, *et al.*, "A broadband achromatic metalens in the visible," Nat. Nanotechnol. **13**, 227 (2018).
5. R. Ahmed and H. Butt, "Strain-multiplex metalens array for tunable focusing and imaging," Adv. Sci. **8**, 2003394 (2021).
6. X. Che, Y. Yu, Z. Gao, *et al.*, "A broadband achromatic Alvarez metalens," Opt. Laser Technol. **159**, 108985 (2023).
7. Q. Xu, X. Su, X. Zhang, *et al.*, "Mechanically reprogrammable Pancharatnam–Berry metasurface for microwaves," Adv. Photonics **4**, 016002 (2022).
8. C. A. Dirdal, P. C. Thrane, F. T. Dullo, *et al.*, "MEMS-tunable dielectric metasurface lens using thin-film PZT for large displacements at low voltages," Opt. Lett. **47**, 1049 (2022).
9. Y. Li, J. Xie, L. Deng, *et al.*, "Active metasurfaces based on phase transition material vanadium dioxide," Sci. China Mater. **66**, 284 (2023).
10. S. Zhu, Q. Jiang, Y. Wang, *et al.*, "Nonmechanical varifocal metalens using nematic liquid crystal," Nanophotonics **12**, 1169 (2023).
11. S. Wei, G. Cao, H. Lin, *et al.*, "A varifocal graphene metalens for broadband zoom imaging covering the entire visible region," ACS Nano **15**, 4769 (2021).
12. M. Jazbinšek and M. Zgonik, "Material tensor parameters of LiNbO3 relevant for electro-and elasto-optics," Appl. Phys. B **74**, 407 (2002).
13. D. Zhu, L. Shao, M. Yu, *et al.*, "Integrated photonics on thin-film lithium niobate," Adv. Opt. Photonics **13**, 242 (2021).
14. C. Wang, M. Zhang, X. Chen, *et al.*, "Integrated lithium niobate electro-optic modulators operating at CMOS-compatible voltages," Nature **562**, 101 (2018).
15. C. Wang, M. Zhang, B. Stern, *et al.*, "Nanophotonic lithium niobate electro-optic modulators," Opt. Express **26**, 1547 (2018).
16. P. Tang, D. Towner, T. Hamano, *et al.*, "Electrooptic modulation up to 40 GHz in a barium titanate thin film waveguide modulator," Opt. Express **12**, 5962 (2004).
17. Q. Xu, B. Schmidt, S. Pradhan, *et al.*, "Micrometre-scale silicon electro-optic modulator," Nature **435**, 325 (2005).
18. F. Ni, H. Li, H. Liu, *et al.*, "High-speed optical pulse shaping based on programmable lithium niobate spatial light modulators," Opt. Lett. **48**, 884 (2023).
19. X. Sun, Y. Wu, C. Lu, *et al.*, "Thin-film lithium niobate polarization modulator without polarization diversity," Opt. Express **30**, 30592 (2022).
20. A. Hoblos, M. Suarez, N. Courjal, *et al.*, "Excitation of symmetry protected modes in a lithium niobate membrane photonic crystal for sensing applications," OSA Contin. **3**, 3008 (2020).
21. M. Roussey, M.-P. Bernal, N. Courjal, *et al.*, "Electro-optic effect exaltation on lithium niobate photonic crystals due to slow photons," Appl. Phys. Lett. **89**, 241110 (2006).
22. M. Roussey, M.-P. Bernal, N. Courjal, *et al.*, "Experimental and theoretical characterization of a lithium niobate photonic crystal," Appl. Phys. Lett. **87**, 241101 (2005).
23. M. Roussey, F. I. Baida, and M.-P. Bernal, "Experimental and theoretical observations of the slow-light effect on a tunable photonic crystal," J. Opt. Soc. Am. B **24**, 1416 (2007).
24. M. Luennemann, U. Hartwig, G. Panotopoulos, *et al.*, "Electrooptic properties of lithium niobate crystals for extremely high external electric fields," Appl. Phys. B **76**, 403 (2003).
25. L. Yang, X. Hong, J. Li, *et al.*, "Rechargeable metasurfaces for dynamic color display based on a compositional and mechanical dual-altered mechanism," Research **2022**, 9828757 (2022).
26. X. Bai, F. Zhang, L. Sun, *et al.*, "Time-modulated transmissive programmable metasurface for low sidelobe beam scanning," Research **2022**, 9825903 (2022).
27. E. Klopfer, S. Dagli, D. Barton, III, *et al.*, "High-quality-factor silicon-on-lithium niobate metasurfaces for electro-optically reconfigurable wavefront shaping," Nano Lett. **22**, 1703 (2022).
28. B. Gao, M. Ren, W. Wu, *et al.*, "Electro-optic lithium niobate metasurfaces," Sci. China Phys. Mech. Astron. **64**, 240362 (2021).
29. A. Weiss, C. Frydendahl, J. Bar-David, *et al.*, "Tunable metasurface using thin-film lithium niobate in the telecom regime," ACS Photonics **9**, 605 (2022).
30. Y. Ju, H. Zhou, Y. Zhao, *et al.*, "Hybrid resonance metasurface for a lithium niobate electro-optical modulator," Opt. Lett. **47**, 5905 (2022).
31. C. Damgaard-Carstensen, M. Thomaschewski, and S. I. Bozhevolnyi, "Electro-optic metasurface-based free-space modulators," Nanoscale **14**, 11407 (2022).
32. C. Damgaard-Carstensen and S. I. Bozhevolnyi, "Nonlocal electro-optic metasurfaces for free-space light modulation," Nanophotonics **12**, 2953 (2023).
33. G. Liu, S. Zong, X. Liu, *et al.*, "High-performance etchless lithium niobate layer electro-optic modulator enabled by quasi-BICs," Opt. Lett. **49**, 113 (2024).

34. J. Liu, L. Qu, W. Wu, *et al.*, "Lithium niobate thin film electro-optic modulator," Nanophotonics **13**, 1503 (2024).
35. C. Damgaard-Carstensen, M. Thomaschewski, F. Ding, *et al.*, "Electrical tuning of Fresnel lens in reflection," ACS Photonics **8**, 1576 (2021).
36. A. Howes, W. Wang, I. Kravchenko, *et al.*, "Dynamic transmission control based on all-dielectric Huygens metasurfaces," Optica **5**, 787 (2018).
37. D. E. Zelmon, D. L. Small, and D. Jundt, "Infrared corrected Sellmeier coefficients for congruently grown lithium niobate and 5 mol. % magnesium oxide–doped lithium niobate," J. Opt. Soc. Am. B **14**, 3319 (1997).
38. B. Yang, W. Liu, Z. Li, *et al.*, "Ultrahighly saturated structural colors enhanced by multipolar-modulated metasurfaces," Nano Lett. **19**, 4221 (2019).
39. R. J. Moerland and J. P. Hoogenboom, "Subnanometer-accuracy optical distance ruler based on fluorescence quenching by transparent conductors," Optica **3**, 112 (2016).
40. R. Weis and T. Gaylord, "Lithium niobate: summary of physical properties and crystal structure," Appl. Phys. A **37**, 191 (1985).
41. D. Mardare and G. Rusu, "Comparison of the dielectric properties for doped and undoped TiO_2 thin films," J. Optoelectron. Adv. Mater. **6**, 333 (2004).
42. M. Born and E. Wolf, *Principles of Optics: Electromagnetic Theory of Propagation, Interference and Diffraction of Light* (Elsevier, 2013).
43. J. Zhong, N. An, N. Yi, *et al.*, "Broadband and tunable-focus flat lens with dielectric metasurface," Plasmonics **11**, 537 (2016).
44. S. C. Malek, A. C. Overvig, S. Shrestha, *et al.*, "Active nonlocal metasurfaces," Nanophotonics **10**, 655 (2020).
45. T. Phan, D. Sell, E. W. Wang, *et al.*, "High-efficiency, large-area, topology-optimized metasurfaces," Light Sci. Appl. **8**, 48 (2019).
46. A. Arbabi, Y. Horie, A. J. Ball, *et al.*, "Subwavelength-thick lenses with high numerical apertures and large efficiency based on high-contrast transmitarrays," Nat. Commun. **6**, 7069 (2015).